Supporting Information

1) Validation of the CRLB

To assess the accuracy of the CRLB as an estimate of parameter variance due to Gaussian noise, we compared the weighted parameter variance (V_W; Equation 23) obtained using either $\mathbf{v}_C = [CRLB_1, \ldots, CRLB_{12}]$ or $\mathbf{v}_C = [V_1, \ldots, V_2]$, where V are variances estimated from simulated distributions of parameter estimates. Data were synthesized using the two-compartment model (Equation 12) and the three prior sets in Table 1, and distributions of parameter estimates were obtained by fitting Equation 12 to 100 realizations of noise from the Gaussian distribution, using the same SNR estimations as in the optimization.

The weighted parameter variance based on either the CRLB or simulations agreed closely, except for the high variance cases of using only LTE ($b_\Delta = 1$) or only four shells (Supporting Information Figure S1). The CLRB and the simulations yielded rather different absolute numbers in those cases, although both indicated an exceptionally high variance. Thus, the CRLB should be able to reject protocols lacking the essential features and allow a more detailed optimization in lower variance regimes.

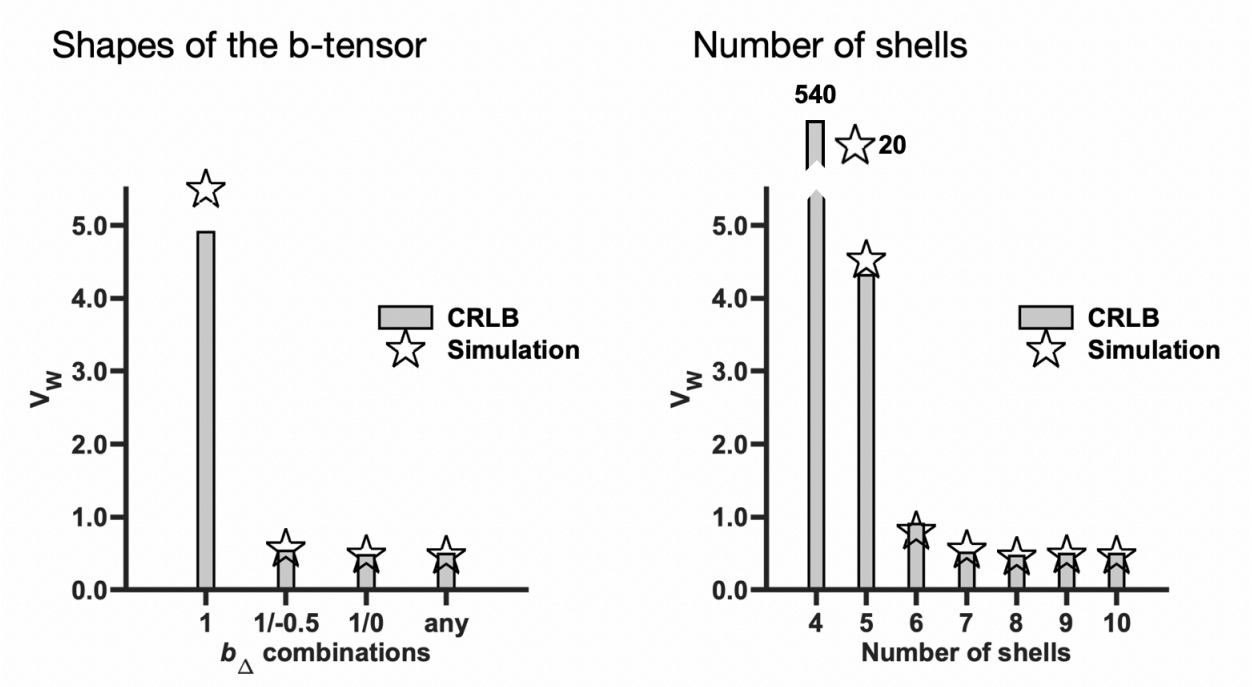

Supporting Information Figure S1 – The weighted parameter variance (V_W) obtained using the CRLB agreed closely with the same metric obtained from simulations. In the cases of using only $b_\Delta = 1$ or only four shells, variances were different but still high. The result suggests that protocol optimization based on the CLRB is a valid approach for minimizing the impact of Gaussian noise.

2) Parameter maps (multi-slice gallery)

This section complements Figure 5 with an extended figure showing parameter maps from multiple slices from the same subject (Supporting Information Figure S2).

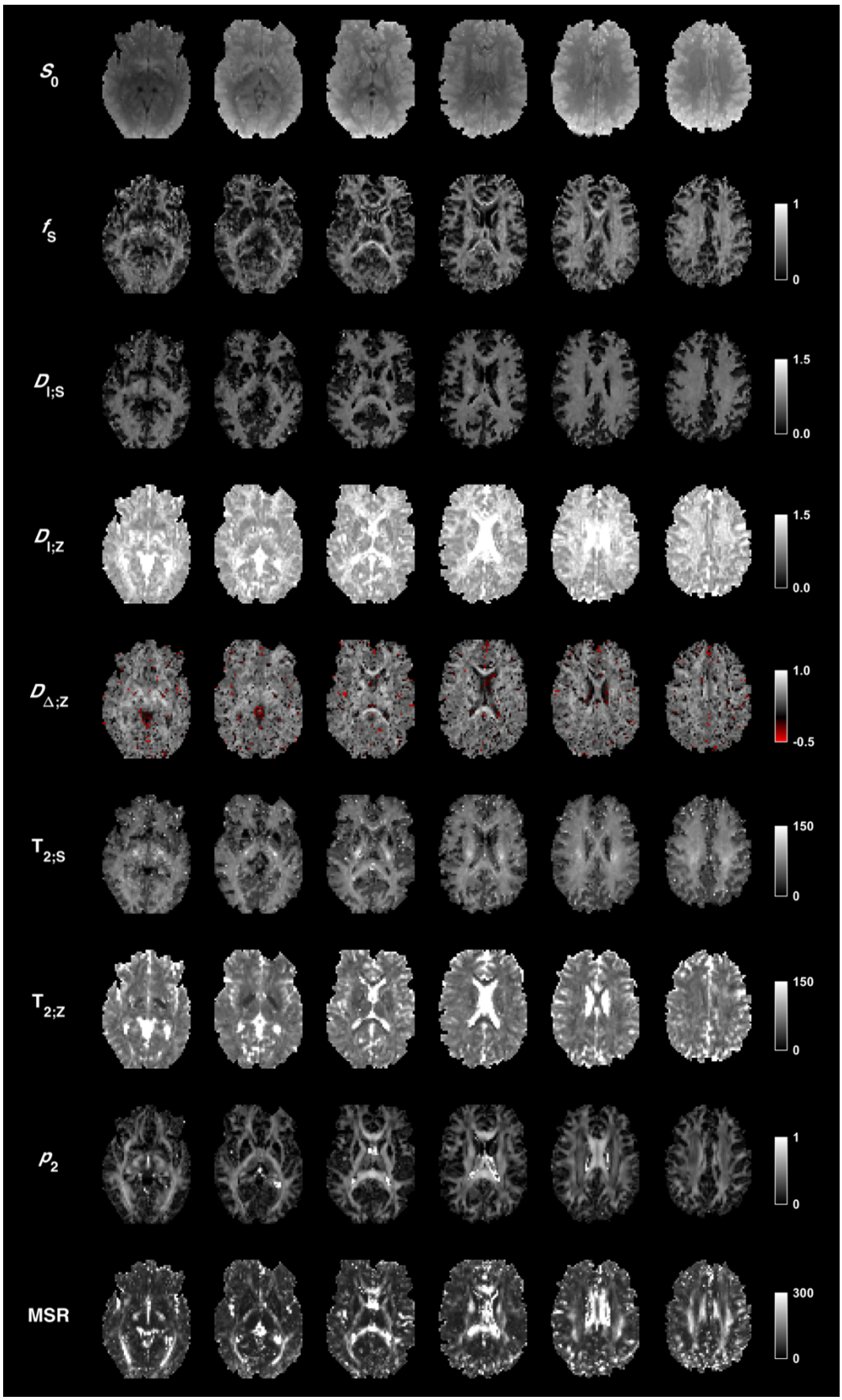
S_0
f_s
1
0
$D_{l;s}$
1.5
0.0
$D_{l;z}$
1.5
0.0
$D_{\Delta;z}$
1.0
-0.5
$T_{2;s}$
150
0
$T_{2;z}$
150
0
p_2
1
0
MSR
300
0

Supporting Information Figure S2 – Multi-slice gallery of the kernel parameters in an adult subject together with p_2 and the mean squared residuals (MSR) from the fitting. Isotropic diffusivities are in $\mu m^2/ms$, T_2 values are in ms and remaining parameters are dimensionless. All maps were masked to exclude voxels outside of the brain. In addition, the $D_{I;S}$, $T_{2;S}$, and p_2 maps were masked to exclude voxels where $f_S < 0.1$. In the $T_{2;S}$ maps, the cerebrospinal tract was visible along its full extent from the brainstem to the motor cortex. In the $T_{2;Z}$ maps, the iron-rich globus pallidus stood out as particularly dark.

3) Parameter repeatability

To analyze parameter repeatability, one adult volunteer was scanned twice consecutively using the in vivo protocol (Table 2, protocol II). To avoid bias from motion or system drift, the two datasets were concatenated and jointly motion-corrected after which consecutive image volumes were alternatingly assigned to one of two new datasets labeled “test” and “retest” (switching order between the two original datasets). Model fitting was performed as described in section 3.2. No smoothing was applied prior to fitting.

Test and retest parameter maps showed essentially the same contrast (Supporting Information Figure S3). Because this data did not undergo smoothing prior to fitting, the maps were noisier than the corresponding maps in Figure 5. The difference maps appeared mostly random but featured some “patches”. For example, negative $D_{\Delta;Z}$ differences were seen near the anterior corona radiata and positive $T_{2;S}$ differences were seen in the right thalamus. Bland-Altman plots of test and retest values within non-cortical brain tissue (Figure 1C) indicated that the bias was small.

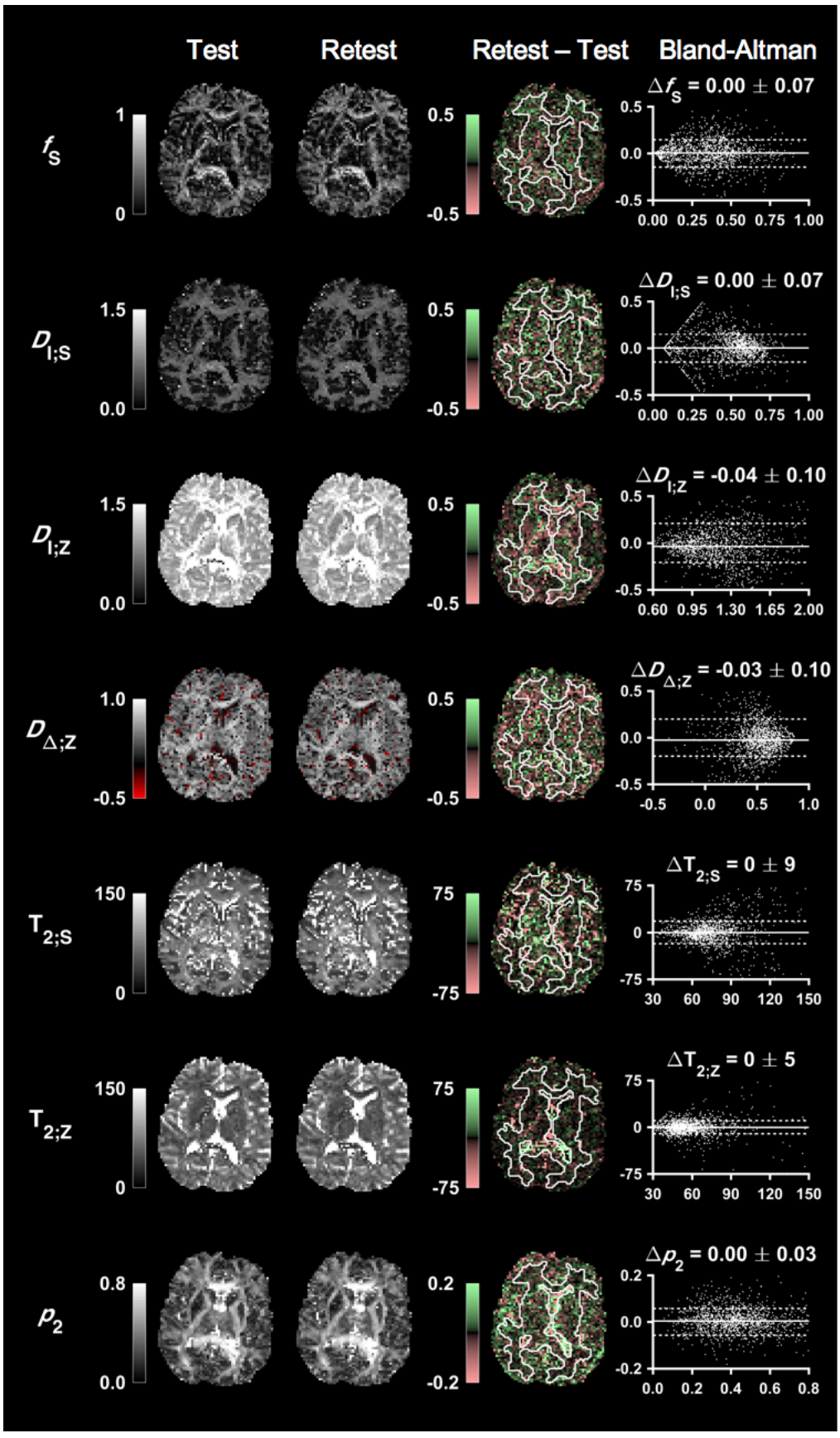
Test
Retest
Retest – Test
Bland-Altman
f_S
1
0
0.5
-0.5
$\Delta f_S = 0.00 \pm 0.07$
0.5
0.0
-0.5
0.00 0.25 0.50 0.75 1.00
$D_{I;S}$
1.5
0.0
0.5
-0.5
$\Delta D_{I;S} = 0.00 \pm 0.07$
0.5
0.0
-0.5
0.00 0.25 0.50 0.75 1.00
$D_{I;Z}$
1.5
0.0
0.5
-0.5
$\Delta D_{I;Z} = -0.04 \pm 0.10$
0.5
0.0
-0.5
0.60 0.95 1.30 1.65 2.00
$D_{\Delta;Z}$
1.0
-0.5
0.5
-0.5
$\Delta D_{\Delta;Z} = -0.03 \pm 0.10$
0.5
0.0
-0.5
-0.5 0.0 0.5 1.0
$T_{2;S}$
150
0
75
-75
$\Delta T_{2;S} = 0 \pm 9$
75
0
-75
30 60 90 120 150
$T_{2;Z}$
150
0
75
-75
$\Delta T_{2;Z} = 0 \pm 5$
75
0
-75
30 60 90 120 150
p_2
0.8
0.0
0.2
-0.2
$\Delta p_2 = 0.00 \pm 0.03$
0.2
0.0
-0.2
0.0 0.2 0.4 0.6 0.8

Supporting Information Figure S3 – Test and retest maps from an adult subject together with difference maps. Bland-Altman plots show mean test-retest values (y-axes) and difference values (x-axes) from within non-cortical brain tissue (white ROI). The numbers denote median ± mean average deviation from the median. Isotropic diffusivities are in $\mu m^2/ms$, T_2 values are in ms and remaining parameters are dimensionless.

4) The importance of the number of shells for the ability to determine all model parameters

To assess the importance of the number of protocol shells (b/b_Δ/TE-combinations) for the ability to determine all model parameters, we studied correlations between parameter estimates when simulated under different levels of orientation dispersion. Data were synthesized for the protocols in Figure 2D restricted to either seven, six, five or four shells. The simulations used prior set A from Table 1, but adjusted to feature either full orientation dispersion (OD = 1, p_2 = 0) or intermediate orientation dispersion (OD = 0.5, p_2 = 0.15). Distributions of parameter estimates were obtained by fitting Equation 12 to 200 realizations of noise from the Gaussian distribution. The SNR was estimated as in the optimization and adjusted for acquisition time as described at the end of section 3.3.

The seven-shell protocol resulted in a well-determined solution even under full orientation dispersion (Supporting Information Figure S4). However, using only six shells resulted in the $D_{\Delta;Z}$ parameter being undetermined, using only five shells resulted in additional bias in multiple parameters (particularly in $D_{I;Z}$), and using only four shells resulted in severe bias in most parameters. Under intermediate orientation dispersion, these issues were resolved for the six- and the five-shell protocols (although parameter precision was still relatively poor) but not for the four-shell protocol (Supporting Information Figure S5). The result indicates that directional information may allow six- or five- shell protocols to determine all parameters under some circumstances, but that robustness to full orientation dispersion at least requires seven shells. Notably, the p_2 parameter was well determined in all simulations.

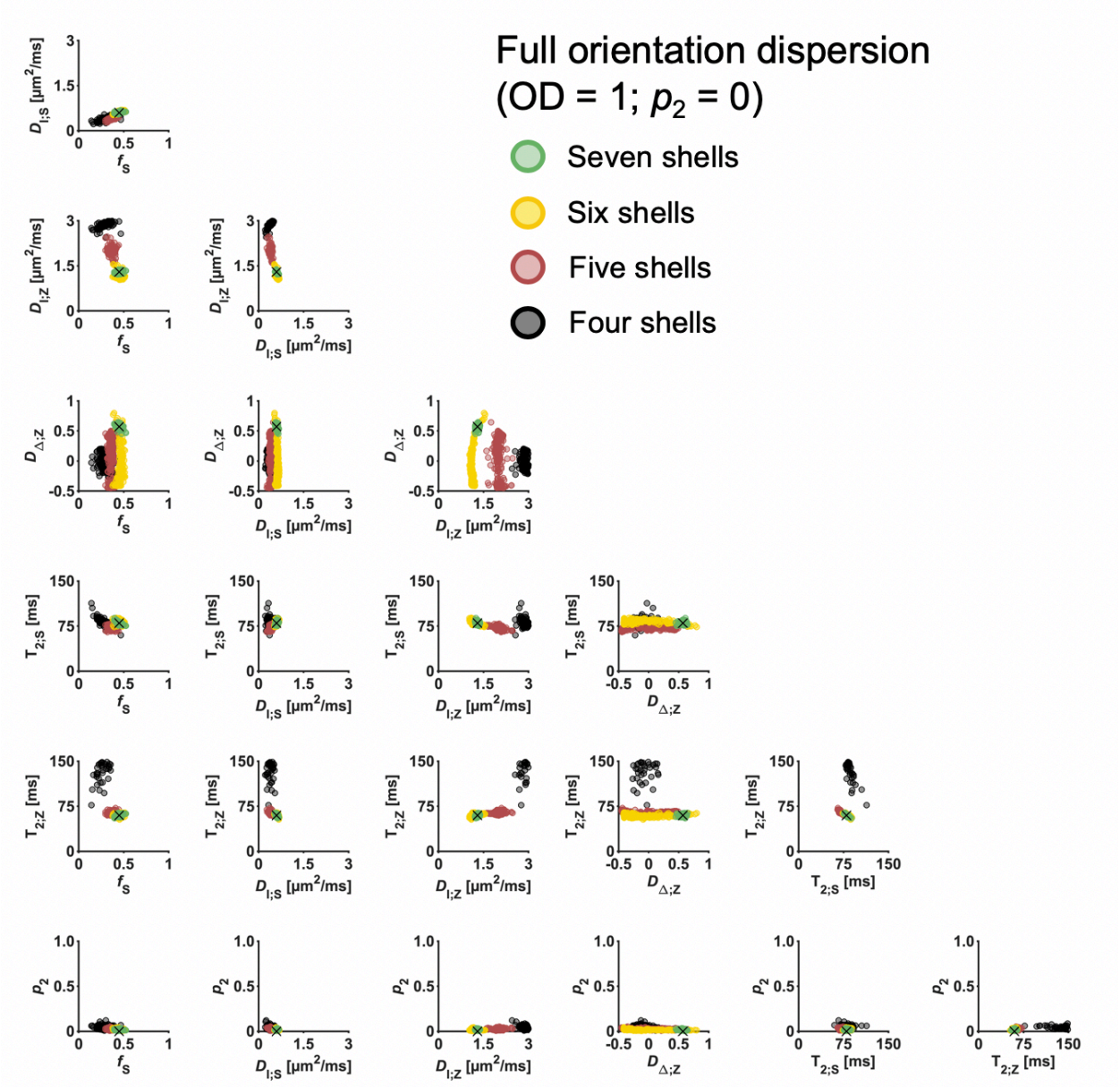

Supporting Information Figure S4 – Correlation plots of estimated parameter values simulated under full orientation dispersion. Crosses indicate ground truth values. Using seven shells was sufficient for a single solution but decreasing the number of shells resulted in the $D_{\Delta;Z}$ parameter being undetermined (six shells) and in increasing bias in most other parameters (five or four shells).

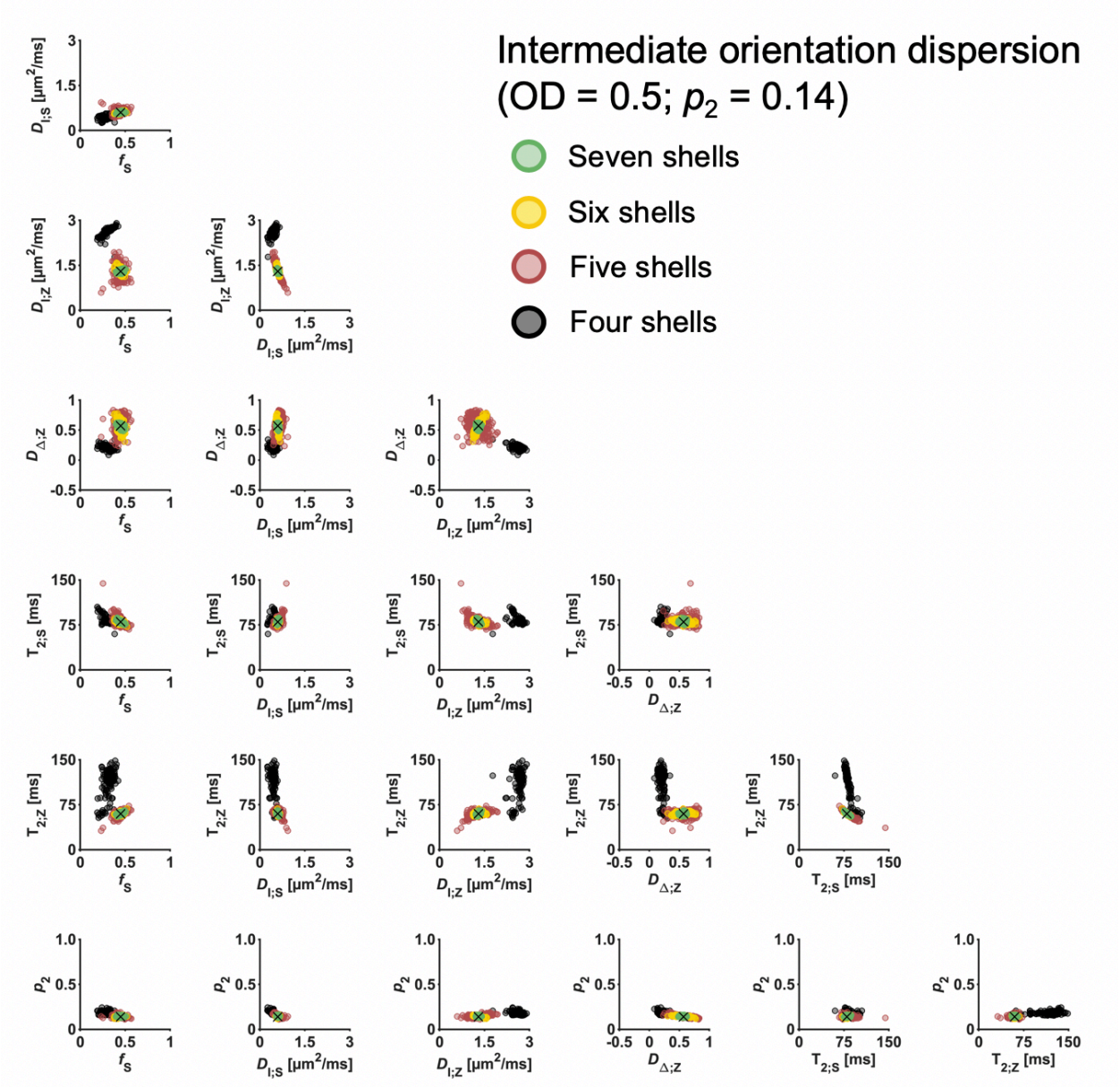

Supporting Information Figure S5 – Correlation plots of estimated parameter values simulated under intermediate orientation dispersion. Crosses indicate ground truth values. The six- and five-shell protocols, but not the four-shell protocol, could determine all parameters without bias when orientation dispersion was not complete (although with poor precision).

5) Investigation of kernel parameter bias from fitting a simplistic ODF

To investigate whether modeling errors from fitting a relatively simplistic ODF may bias kernel parameters, we compared the parameter estimates obtained with the herein used approach to those obtained using the "RotInv" approach.[1-3] Rather than fitting a forward model directly to the signal, as done in this work (Equation 12), an alternative approach is to project the signal onto the relevant harmonic orders and fit the coefficients of the model to those of the signal. Equation 4 can be expressed as

$$S(\mathbf{u}) = \sum_l \sum_m k_{l0}\, p_{lm}\, Y_{lm}(\mathbf{u}) \sqrt{\frac{4\pi}{2l+1}} = \sum_l \sum_m S_{lm} Y_{lm}(\mathbf{u}), \tag{S1}$$

where S_{lm} are the spherical harmonic coefficients of the signal obtained by projection onto the corresponding basis function, according to $S_{lm} = \langle S|Y_{lm}\rangle$ (Equation 6). To mimic the RotInv approach, we minimized an objective function of the form

$$\mathrm{OF} = \sum_{l=0,2} \|S_l - k_l \cdot p_l\|^2, \tag{S2}$$

where the rotational invariants S_2 and p_2 were obtained using p_{2m} and S_{2m} in Equation 15, respectively. With this approach, the modeling errors from using a simple ODF should manifest as residuals in the projections $\langle S|Y_{lm}\rangle$ rather than in the full model fit, wherefore their impact on the estimated kernel parameters should be minimized.

Supporting Information Figure S6 shows that the herein used approach (Direct) and the RotInv approach yielded nearly identical maps of the kernel parameters (and p_2), featuring the same contrast and general intensity and indicating similar precision. The difference maps and the Bland-Altman plots indicated a very small negative bias in the $D_{\Delta;Z}$ parameter but otherwise a negligible bias in the kernel parameters. The result suggests that fitting a forward model using a simple ODF directly to the signal has limited effect on the kernel parameters even though the fit residuals may be large in orientationally coherent regions such as the corpus callosum (Figure 5, MSR).

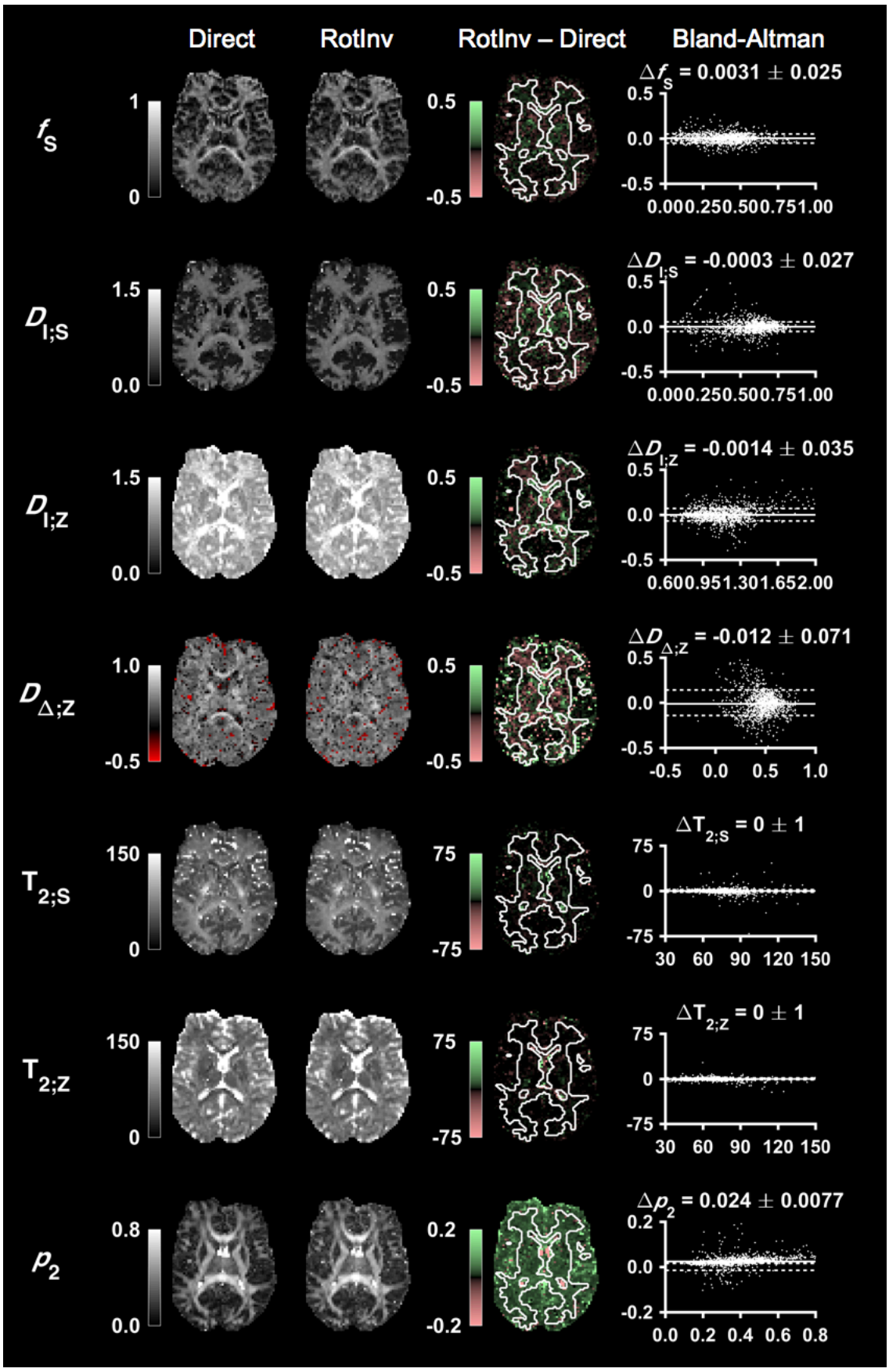
Direct
RotInv
RotInv – Direct
Bland-Altman
f_S
1
0
0.5
-0.5
Δf_S = 0.0031 ± 0.025
0.5
0.0
-0.5
0.000.250.500.751.00
$D_{I;S}$
1.5
0.0
0.5
-0.5
$\Delta D_{I;S}$ = -0.0003 ± 0.027
0.5
0.0
-0.5
0.000.250.500.751.00
$D_{I;Z}$
1.5
0.0
0.5
-0.5
$\Delta D_{I;Z}$ = -0.0014 ± 0.035
0.5
0.0
-0.5
0.600.951.301.652.00
$D_{\Delta;Z}$
1.0
-0.5
0.5
-0.5
$\Delta D_{\Delta;Z}$ = -0.012 ± 0.071
0.5
0.0
-0.5
-0.5 0.0 0.5 1.0
$T_{2;S}$
150
0
75
-75
$\Delta T_{2;S}$ = 0 ± 1
75
0
-75
30 60 90 120 150
$T_{2;Z}$
150
0
75
-75
$\Delta T_{2;Z}$ = 0 ± 1
75
0
-75
30 60 90 120 150
p_2
0.8
0.0
0.2
-0.2
Δp_2 = 0.024 ± 0.0077
0.2
0.0
-0.2
0.0 0.2 0.4 0.6 0.8

Supporting Information Figure S6 – Comparison of parameter maps obtained by fitting Equation 12 to the raw data (Direct) versus minimizing the objective function in Equation S2 (RotInv). Bland-Altman plots show mean values (y-axes) and difference values (x-axes) from within non-cortical brain tissue (white ROI). The numbers denote median ± mean average deviation from the median. Isotropic diffusivities are in $\mu m^2/ms$, T_2 values are in ms and remaining parameters are dimensionless.

6) Including a free water compartment

To explore the inclusion of a free water compartment, we fitted an extended model given by

$$S' = (1 - f_{\mathrm{FW}}) \cdot S + f_{\mathrm{FW}} \cdot e^{-bD_{\mathrm{I;FW}}} \cdot e^{-\frac{\mathrm{TE}}{\mathrm{T_{2;FW}}}}, \quad \text{(S3)}$$

where S is given by Equation 12, $f_{\mathrm{FW}} \in [0\ 1]$ is the free water fraction, $D_{\mathrm{I;FW}}$ = 3.0 μm^2/ms and $T_{2;FW}$ = 1400 ms. Fitting was performed to the data from one adult subject within one slice as described in section 3.2 but with the upper bound of $T_{2;NS}$ adjusted to 300 ms. For extracting parameter values, we used the non-cortical brain mask (Figure 1C) together with a cortical mask defined as voxels within a whole-brain mask but outside the non-cortical brain mask and featuring FA < 0.25 and MD > 1.0 μm^2/ms.

A map of the f_{FW} parameter is shown in Supporting Information Figure S7 panel A, together with regional values within the non-cortical brain and the cortex. The f_{FW} map yielded a plausible definition of the CSF-rich regions of the brain, being bright within the ventricles and in cortical voxels close to the sulci. Average f_{FW} values were close to zero within non-cortical brain tissue, a few percent within the cortex, and approximately unity within the ventricles (not shown). The effect on the other parameters from including a free water compartment is shown in panel B. Within the non-cortical brain (red ROI), parameter maps were not appreciably noisier and featured close to the same contrast. The difference maps and the Bland-Altman plots revealed a small effect on some parameter averages. In particular, $T_{2;S}$ was higher while f_S, $D_{\mathrm{I;Z}}$ and $T_{2;Z}$ were lower. Within the cortex, the maps describing the "stick" properties ($D_{\mathrm{I;S}}$ and $T_{2;S}$) were somewhat noisier, likely reflecting a lower f_S. Also, the maps describing the "zeppelin" properties ($D_{\mathrm{I;Z}}$ and $T_{2;Z}$) featured a flatter contrast, likely due to signal previously captured in this compartment now being captured in the free water compartment. The average parameter values were affected in the same direction as observed in the non-cortical brain, although more parameters were affected and the effects were larger.

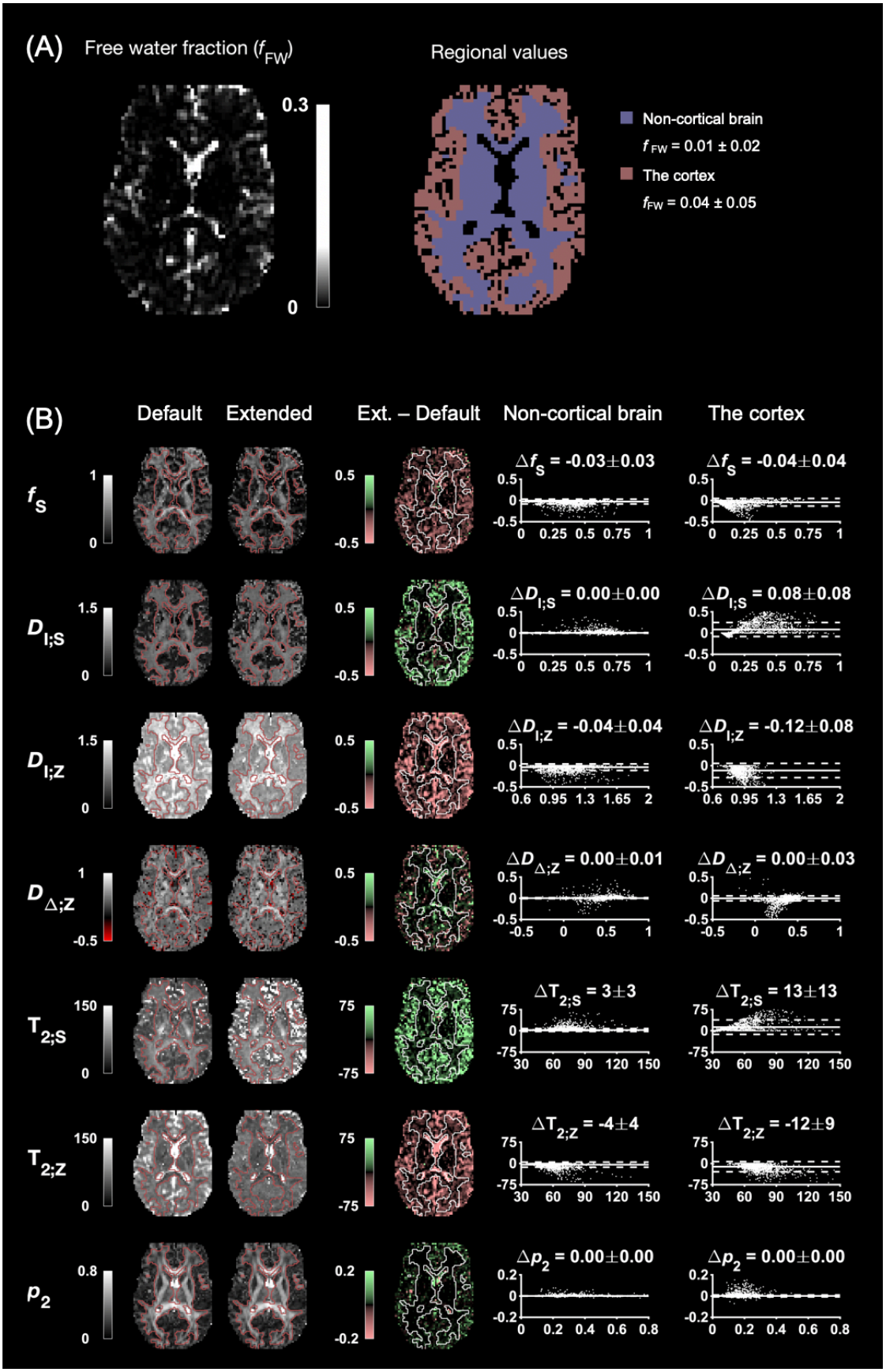
(A)
Free water fraction (f_{FW})
0.3
0
Regional values
Non-cortical brain
f_{FW} = 0.01 ± 0.02
The cortex
f_{FW} = 0.04 ± 0.05
(B)
Default
Extended
Ext. – Default
Non-cortical brain
The cortex
f_S
Δf_S = -0.03±0.03
Δf_S = -0.04±0.04
$D_{I;S}$
$\Delta D_{I;S}$ = 0.00±0.00
$\Delta D_{I;S}$ = 0.08±0.08
$D_{I;Z}$
$\Delta D_{I;Z}$ = -0.04±0.04
$\Delta D_{I;Z}$ = -0.12±0.08
$D_{\Delta;Z}$
$\Delta D_{\Delta;Z}$ = 0.00±0.01
$\Delta D_{\Delta;Z}$ = 0.00±0.03
$T_{2;S}$
$\Delta T_{2;S}$ = 3±3
$\Delta T_{2;S}$ = 13±13
$T_{2;Z}$
$\Delta T_{2;Z}$ = -4±4
$\Delta T_{2;Z}$ = -12±9
p_2
Δp_2 = 0.00±0.00
Δp_2 = 0.00±0.00

Supporting Information Figure S7 – Panel A shows a free water fraction (f_{FW}) map together with regional values within masks of the non-cortical brain and the cortex (mean ± standard deviation). Panel B shows the effect of including a free water compartment on maps of the other parameters. The maps from the extended model were not appreciably noisier, suggesting that the data yielded by the in vivo protocol may support models with higher capacity than the herein used two-compartment model. Introducing the f_{FW} parameter did not visibly affect the contrast within the non-cortical brain, but yielded maps with flatter contrast within the cortex for the "zeppelin" properties ($D_{I;Z}$ and $T_{2;Z}$). The difference maps and the Bland-Altman plots (showing differences on y-axis and means on x-axis for voxels within the shown slice) show that the average parameter values were affected across the whole brain, but particularly in the cortex. The numbers denote median ± mean average deviation from the median. Isotropic diffusivities are in $\mu m^2/ms$, T_2 values are in ms and remaining parameters are dimensionless.

1 Novikov, D. S., Veraart, J., Jelescu, I. O. & Fieremans, E. Rotationally-invariant mapping of scalar and orientational metrics of neuronal microstructure with diffusion MRI. *Neuroimage* **174**, 518-538 (2018).

2 Reisert, M., Kellner, E., Dhital, B., Hennig, J. & Kiselev, V. G. J. N. Disentangling micro from mesostructure by diffusion MRI: A Bayesian approach. **147**, 964-975 (2017).

3 Veraart, J., Novikov, D. S. & Fieremans, E. TE dependent Diffusion Imaging (TEdDI) distinguishes between compartmental T2 relaxation times. *Neuroimage* **182**, 360-369 (2017).